AIAA 2005-0527

Multicomponent and Unsteady Velocity Measurements of Transient Disturbances

F. Gökhan Ergin* and Edward B. White†
Mechanical and Aerospace Engineering
Case Western Reserve University
Cleveland, OH 44106

Two experiments are conducted to investigate transient growth and bypass transition in boundary layers with moderate- to high-amplitude roughness arrays. Unsteady and multicomponent velocity measurements are obtained in a flat plate boundary layer downstream of a spanwise array of cylindrical roughness elements with roughness Reynolds numbers of Re_k = 202, 264 and 334. Measurements of the unsteady streamwise velocities in the wake indicate that growth of a 720 Hz fluctuation leads rapidly to bypass transition at Re_k = 334. The Strouhal number of this fluctuation, St = 0.17, is in good agreement with previous experiments. The locations of maximum fluctuation intensity suggest that the fluctuations result from a Kelvin–Helmholz-type instability of the spanwise-varying wake. Additionally, steady spanwise velocities are measured in an effort to supply the initial conditions for the downstream transient growth of the streamwise velocity disturbance. Time-averaged streamwise and spanwise velocity components are measured using a combination of multiple slanted and straight hotwire sensors. The multicomponent measurements reveal the expected horseshoe vortex structure that is symmetric around the roughness centerline.

I. Introduction

Transient disturbance growth in boundary layers is a mechanism that may describe transition scenarios that lie between classical Tollmien–Schlichting (TS) transition that occurs in low-disturbance environments and bypass transition in high-disturbance environments. Briefly, transient growth is the algebraic growth and exponential decay of disturbances generated by three-dimensional (3D) sources such as freestream turbulence and surface roughness. This mechanism was first identified by Ellingsen and Palm (1975) and Landahl (1980) as an inviscid mechanism of algebraic kinetic energy growth in shear layers. The physical picture of transient growth can be described using Landahl's (1980) "lift-up" mechanism, the process through which a weakly damped streamwise-oriented vortex transfers high-velocity fluid from the top of the boundary layer to the lower part and simultaneously transfers low-velocity fluid from the bottom of the boundary layer to the upper part. This action creates an algebraically growing perturbation of the streamwise velocity that consists of high- and low-speed longitudinal streaks. However, the streamwise vortex is stable and decays. Once it disappears, the streamwise velocity disturbance cannot be sustained and this too undergoes exponential decay.

The mathematical foundations of transient growth are discussed by Schmid and Henningson (2001) and Reshotko (2001) who describe that transient growth arises because the linearized disturbance equations are not self-adjoint and, therefore, have nonorthogonal eigenmodes. In boundary layers, disturbances are represented by the superposition of the Orr–Sommerfeld equation's discrete and continuous spectrum of eigenmodes. (For a detailed analysis of continuous spectrum concept see the articles by Grosch and Salwen 1978 and Ashpis and Reshotko 1990; 1998.) In classical TS stability analysis, the most unstable discrete eigenmode represents the observed disturbance growth. However, in the subcritical region where no TS waves are unstable, the superposition of continuous spectrum is essential for explaining transient disturbances. Because each continuous mode decays at a different rate, a disturbance that is represented by nearly canceling modes may grow as some modes decay more quickly than others and upset the initial cancellation. Different combinations of eigenmodes lead to different transient growth characteristics for the same

*Ph.D. Candidate, AIAA Member
†Asst. Professor, AIAA Senior Member

disturbance wavenumbers and frequencies. For any combination of spanwise wavenumber and frequency one initial disturbance leads to maximum disturbance growth and this is known as the optimal disturbance (Farrell 1988). Optimal 3D disturbances in boundary layers have been investigated by Butler and Farrell (1992), Andersson et al. (1999), Luchini (2000) and Tumin and Reshotko (2001).

Experiments on roughness-induced transient growth have been performed by White and coworkers (White and Reshotko 2002; White 2002; White and Ergin 2003; White et al. 2005) at Case Western Reserve University (Case) and by Fransson et al. (2004) at KTH. The main conclusion of these studies is that surface roughness produces stationary disturbances that undergo transient growth but that this growth is strongly non-optimal. Moreover, the nature of the non-optimal behavior is extremely sensitive to details of the roughness configuration (White et al. 2005). The implication is that if one is to accurately predict transient growth of physically realizable (i.e., not optimal) disturbances, initial conditions need to be determined. Fischer and Choudhari (2004) have performed a DNS of White and Ergin's (2003) experiment and achieved remarkable agreement with the experimental data. However a DNS is costly and it would be preferable to obtain initial conditions using other methods. Tumin (2003) proposes a method for calculating amplitudes of discretized eigenmodes of the continuous spectrum from data using a biorthogonality principle and this could be a means of generating the desired initial conditions. However, Tumin's method requires knowledge of the complete disturbance field and this has not yet been measured in an experiment.

In addition to investigating variations in non-optimality, White et al. (2005) also examined the role of roughness amplitude. The finding is that the energy of a stationary transient disturbance initiated by a roughness array scales as Re_k^2 (i.e., as k^4); that is, the receptivity is nonlinear. The quadratic energy scaling appears to hold from $Re_k = 16$ (the smallest amplitude that produces a measurable disturbance) to $Re_k = 254$. Beyond $Re_k = 254$, Rice (2004) observed unsteady bypass transition in the roughness array's wake. This bypass is thought to be similar to the high-amplitude, isolated-roughness transition scenarios investigated by Acarlar and Smith (1987) using flow visualization, by Klebanoff et al. (1992) using hotwire anemometry and numerous earlier investigators including Dryden and Tani. (Early references are given in the review by Sedney 1973.)

Studies of transitional flows over large-amplitude roughness elements that do not explicitly consider transient growth provide an important background to two outstanding questions about roughness-induced transient growth. First, beyond what roughness amplitudes is transient growth *not* observed because of rapid bypass transition and what is the mechanism for this transition? Second, if bypass does not occur, how is the topology of the flow over the roughness element associated with the streamwise vortex that is the initial condition for transient growth? On the first point, it is suspected that the unsteady hairpin vortices shed from the high-amplitude roughness elements are what led to the bypass observed by Rice (2004). On the second point, the steady horseshoe vortex that is shown in photographs and sketches by Acarlar and Smith (1987) may provide the initial streamwise vorticity that leads to transient growth. A sketch of the horseshoe vortex is given in Fig. 1. If this vortex does exist in the roughness-array configurations considered in recent experiments, measurements of the spanwise velocity in the array's wake should resemble the profiles indicated in the measurement plane on the right side of the figure.

The objective of the present paper is to continue the investigations at Case that are aimed at developing a better understanding of roughness-induced transition and, in particular, to address the two questions raised above. This is done in two separate experiments: one that includes measurements of unsteady streamwise velocities and one that includes measurements of multicomponent (streamwise and spanwise) velocities. The main data analysis technique used previously at Case was to measure the steady streamwise disturbances, decompose these into spanwise wavelength components using a spanwise Fourier transform, and monitor each component's downstream evolution. The present work extends this by including measurements of the unsteady fluctuations in the wake of large-amplitude roughness. Temporal Fourier transforms are performed to investigate the fluctuations' frequency characteristics. The multicomponent measurements are a preliminary experiment aimed at obtaining the data that is required as input to Tumin's (2003) biorthogonal decomposition. In the long term, multicomponent measurements will provide the initial conditions that are required for predictions of physically realizable transient growth.

II. Experiments and Data Analysis

The current experiments closely follow the previous work by White and coworkers in terms of experimental setup. The facility used for the experiments is the Case Wind Tunnel, an open-return facility with a 0.71 m$\times$0.71 m$\times$2.7 m test section and a maximum operation speed of 25 m/s. The test section features an externally-mounted, computer-controlled hotwire traverse mechanism with microstepping motors that move the sensors in three perpendicular direc-

tions. The tunnel provides a low disturbance level for sensitive boundary-layer stability experiments. Restricted to a high-pass frequency of 1 Hz the turbulent $u'_{\rm rms}$ level is 0.05% of the freestream speed.

Measurements are obtained in the boundary layer of a flat aluminum plate that is polished to a near-mirror finish and has a 25-mm-long elliptical leading edge. The stagnation streamline is controlled by a 300-mm-long trailing-edge flap. The boundary layer's virtual leading edge location and the effective unit Reynolds number are estimated using a nonlinear least-squares fit to the boundary-layer thickness as a function of streamwise position. At the experiments' nominal freestream speed of 12.2 m/s, the unit Reynolds number is $Re' = 764\times10^3$ m^{-1} and the virtual leading edge location is at $x = -7$ mm (upstream of the physical leading edge). Great care is exercised in the alignment of the flat plate. This is essential both to ensure a zero-pressure-gradient flow and for the multicomponent velocity measurements. Measurements show that the smooth-plate shape factor is $H = 2.56$, so the flow is very slightly accelerated but within an acceptable deviation from the zero-pressure-gradient value, $H = 2.59$.

Disturbances are generated by a spanwise array of cylindrical roughness elements. Roughness arrays are advantageous because they generate controlled disturbance inputs that permit the use of various data reduction techniques, especially spatial phase-locked averaging, that greatly improve the signal-to-noise characteristics of the data. The roughness elements consist of 6.35-mm-diameter, 101.6-μm-thick adhesive-backed labels that are stacked to provide desired roughness heights. For both the unsteady and multicomponent experiments the roughness elements are placed 300 mm downstream of the physical leading edge and are spaced 19 mm apart in the spanwise (z) direction. This spacing is referred to as λ_k.

A. Unsteady Data Acquisition and Analysis

The previous experiments at Case consisted of time-averaged streamwise velocity measurements only. The present work provides the unsteady velocity data to explore frequency characteristics of the transient disturbances at higher values of Re_k. For unsteady measurements, 710-, 815- and 915-μm-high roughness elements are used to yield roughness Reynolds number of $Re_k = 202$, 264 and 334. An array of 12 of these elements is applied on the surface but the spanwise measurement range covers only 8 elements in the middle of the array.

The hotwire velocity measurements are performed in planes perpendicular to the flow direction. Two straight-wire sensors are used to measure the boundary layer and freestream velocities simultaneously. In each measurement plane the spanwise movements of the hotwire probes are constant; the 19 mm spacing is covered in 12 steps. The wall-normal step is variable with 400-μm steps outside the boundary layer (starting at approximately $\eta = 8$) and progressively smaller steps within the boundary layer until a cut-off velocity is reached and the sensors are moved away from the plate to their original position. This scanning technique is similar to what White (2002) used, however the wall-location estimation algorithm has been adjusted to avoid errors that affected earlier results (see White and Ergin 2004).

At each measurement location, the velocity is sampled at 10 kHz. The signal is divided into a number of segments with 1024 data points, which allows the use of an FFT algorithm. The number of segments increases from 8 to 12 to 18 as the boundary layer sensor approaches to the flat surface so that the measurements closest to the wall are well resolved without requiring that all points be sampled as extensively. In order to reduce post-experiment data analysis and computer storage requirements, the segments are Fourier transformed individually as the experiment proceeds. After the first segment of data is obtained, it is transformed while the second segment is being gathered. The average of the individual transforms is computed and the one-sided, magnitude-averaged, temporal power spectral density (PSD) of that particular measurement location is given by

$$\mathrm{PSD}(f_n) = \frac{2H_n^2}{f_{\rm samp} W_{ss}}.$$

In this equation, f_n is the nth frequency, H_n are the discrete Fourier coefficients, $f_{\rm samp}$ is the sampling frequency (10 kHz) and W_{ss} is the Hanning window squared and summed as defined by Press et al. (1992). This particular expression for the PSD is selected so that a numerical integration of PSD over the frequency domain is equal to ${u'_{\rm rms}}^2$.

B. Multicomponent Data Acquisition and Analysis

Tumin's (2003) decomposition method requires knowledge of the complete disturbance field including the pressure disturbance, all three velocity components' disturbances and their derivatives. Obtaining the complete disturbance in-

formation is trivial in computational studies because this information exists as part of the numerical solution. However, in an experiment, it is extremely difficult to measure the wall-normal velocity disturbances and perhaps impossible to measure wall-normal pressure-disturbance profiles. Fortunately, partial disturbance field information, excluding pressure, can be used to decompose the flow field into a finite number of discretized eigenmodes if the disturbance consists of downstream vorticity eigenmodes only (Tumin 2003). For stationary transient disturbances these are the only modes that are thought to be important. One goal of the ongoing work at Case is to obtain the complete multi-component velocity disturbance field and to use this information as an input to Tumin's biorthogonal decomposition procedure. To do this, streamwise and spanwise disturbances will be measured and wall-normal disturbances will be estimated using the continuity equation. In this preliminary work, simply measuring the streamwise and spanwise disturbances is the objective.

Measuring the spanwise velocity requires the placement of at least two slanted hotwires with different angular orientations at the same location. For this purpose, a new hotwire sting design is used that carries a combination of slanted and straight hotwire sensors. This sting assembly includes a shaft that rotates in a streamlined casing and allows angular calibration of slanted hotwires. Outside the test section, the shaft is connected to an angle indicator and the sting assembly is rigidly attached to the traverse. Inside the test section, the hotwire sensors are placed perpendicular to the shaft's axis through a multiple-hotwire holder. The angular position of the sensors can be adjusted by rotating the spindle of the angle controller with a precision of 0.2°. The multiple-hotwire holder is designed to carry four hotwires. One hotwire is a straight sensor in the freestream; the remaining three sensors are in the boundary layer. The boundary-layer sensors are positioned in a trident design with one straight sensor in the middle and two slanted hotwire sensors mounted 9.5 mm one either side of the the center probe. Using a separation that is an integer multiple of the spanwise step permits all three boundary layer sensors to be placed at the same measurement location at three different spanwise traverse steps. Naturally, this requires excellent alignment of the flat surface with the traverse plane and the sensors with respect to each other and great care is exercised to achieve this alignment.

Slanted hotwire angle calibration is performed following the recommendations of Bruun (1995). First, the yaw angle of each wire is determined by gradually rotating the sensor in the freestream and monitoring the bridge voltage. When the bridge voltage is a maximum, the maximum cooling rate is achieved because the impinging velocity is perpendicular to the wire axis. The calibration of all four sensors is performed simultaneously. First, the sting is positioned so that all hotwires are located in the freestream. Second, it is rotated 5° clockwise from its position during an experiment and a velocity calibration is performed. Third, the sting is rotated 10° counterclockwise and another velocity calibration is performed for the same tunnel speed range. Finally, data from both velocity calibrations at two different angles are combined and the calibration constants are computed by using the King's Law and Hinze's formula (Hinze 1959):

$$V_e = \left(A + BE^2\right)^n = \tilde{V}\left(\cos^2\alpha + k^2\sin^2\alpha\right)^{1/2}.$$

In these equations A, B and n are calibration constants, $\tilde{V}$ is the freestream speed (during the calibration procedure only), V_e is the effective cooling velocity, E is the hotwire voltage, α is the sensor's yaw angle and k is the sensor's yaw coefficient. A nonlinear least-square fit is performed to find A, B, n and k values for each sensor. The yaw coefficient is assumed to be constant following Jørgensen (1971). According to Bruun, this method predicts the effective cooling velocity to within 1% for yaw angles between 0° and 70° and the error reaches only 15% for a yaw angle of 90°.

For the multicomponent velocity measurements, the roughness array with $Re_k = 202$ elements are used. The approach to hotwire probe movement is similar to what is used by White and Ergin (2003) and White et al. (2005). Briefly, the sensors are positioned outside the boundary layer, they are moved in the spanwise direction with a spanwise step of 0.5 mm (38 steps per λ_k). Spanwise steps proceed until each individual sensor covers the wake of the array's four central elements. Once the spanwise range is completed, the sensors are moved closer to the flat surface, again with a variable y step, and the spanwise scan is repeated. The entire process repeats until the average streamwise velocity for a single y position falls below a cutoff velocity. Effective cooling velocities and yaw coefficients for both slanted sensors are recorded during data acquisition for further analysis.

Multicomponent data is analyzed by decomposing the steady streamwise and spanwise velocity fields into a steady, spanwise-invariant basic state and a steady disturbance as

$$\begin{aligned} U(x,y,z) &= \overline{U}(x,y) + U'(x,y,z) \\ W(x,y,z) &= \overline{W}(x,y) + W'(x,y,z) \end{aligned}$$

Although the basic state for a flat plate is the Blasius boundary layer profile, the present work uses an appropriate experimental basic state which is the average of the boundary layer profiles at the midpoint of two roughness elements. This basic state is assumed to be 2D and, therefore, $\overline{W} = 0$.

The position of each sensor with respect to the flat surface is extremely important for multicomponent data analysis. To account for any misalignment of sensors in the wall-normal direction, the wall location is estimated for each sensor at between-roughness z stations. The normalized boundary layer velocity profile obtained from the middle (normal) sensor is used to calculate the displacement thickness δ^* which in turn gives δ and this nondimensionalizes the wall normal position as $\eta = y/\delta$. The effective cooling velocity obtained from all three sensors are interpolated onto a single array of heights. Once this is completed, the spanwise and streamwise velocities are resolved from the effective cooling velocity data obtained from the slanted sensors. The effective cooling velocity of a hotwire yawed in a 2D flow is given by Hinze's formula, $V_e^2 = U_n^2 + k^2 U_t^2$. In this equation U_n and U_t are the normal and tangential velocity components on each slanted wire. In the present case, the flow has U and W components and $U_n = U\cos\alpha - W\sin\alpha$ and $U_t = U\sin\alpha + W\cos\alpha$. The two slant wires have $\alpha = +46^\circ$ and -38° and, therefore, combining measurements of a single point from the two slant wires provides U and W.

Other experimental procedures and data analysis tools related to steady velocity data are very similar to the previous works at Case (see, e.g., White and Ergin 2003; White et al. 2005). Briefly, the experimental basic state is chosen as the average of the between-element velocity profiles and these profiles are used to calculate the displacement and momentum thickness for each streamwise location. The spanwise rms disturbance of the U velocities ($U'_{\rm rms}$) is obtained from the deviation of phase-lock-averaged velocity profiles from the experimental basic state. The steady velocity field is spatially Fourier transformed to obtain the spatial PSD(λ) profiles. Data windowing and averaging techniques are used to reduce the variance of the spatial power spectrum.

III. Results and Discussion

The baseline configuration for the present work is the roughness configuration with $Re_k = 202$, which produces strong enough disturbances that allows both unsteady and multicomponent velocity measurements. To begin, Fig. 2 gives the basic state and steady disturbance profile at $x = 310$ mm. The thick solid line represents the experimental basic state and is in exellent agreement with the Blasius profile. The agreement between the experimental and theoretical basic state profiles is consistent throughout the streamwise domain. Also included in Fig. 2 is the streamwise rms disturbance profile, $U'_{\rm rms}$, the root-mean-square deviation of the spatially phase-locked-averaged, steady velocity profiles from the experimental basic state. $U'_{\rm rms}$ reaches a maximum of approximately 8.5% of U_∞ around $\eta = 1$ which is consistent with the previous results with similar Re_k values.

The total steady disturbance energy, $E_{\rm rms}$, is obtained by integrating the steady disturbance energy, ${U'_{\rm rms}}^2$ from $\eta = 0$ to the freestream. The downstream evolution of total steady disturbance energy for all three roughness amplitudes is shown in Fig. 3. In all configurations the total disturbance energy decreases rapidly just aft of the roughness elements followed by a slow increase farther downstream. In the $Re_k = 202$ and 264 configurations this increase fades and the total disturbance energy remains roughly constant throughout the remaining streamwise domain. This general behavior is consistent with the previous results of White and Ergin (2003). However, for $Re_k = 334$ the steady disturbance energy undergoes a second decrease beginning at $x = 425$ mm. This occurs because the roughness is of sufficient amplitude to trip the boundary layer. The resulting turbulent mixing reduces the spanwise velocity gradients and, consequentially, the steady disturbance energy. The flow is observed to be completely turbulent downstream of $x = 475$ mm.

A. Unsteady Disturbances

The unsteady disturbance field generated by surface roughness is observed by monitoring the downstream evolution of the fluctuation intensity. Figure 4 shows both the steady and unsteady disturbance field for the baseline $Re_k = 202$ configuration at $x = 310$, 350, 400 and 500 mm. Although data is available behind eight roughness elements only half of those are presented for better visualization. The colored contours in this figure indicate the temporal $u'_{\rm rms}$ velocity fluctuation intensity. (The contours levels follow an exponential distribution so that wide variations in $u'_{\rm rms}$ can be visualized.) The maximum value of $u'_{\rm rms}$ in this figure is 0.4% of U_∞. Overlaid on the unsteady fluctuation contours are the steady U velocity contour lines. In the near wake at $x = 310$ mm, the fluctuations are weak and concentrated in lobes above and downstream of the spanwise edges of the roughness elements. Moving downstream to $x = 350$ mm the fluctuations become stronger and cover a wider spanwise region. The lobes evolve into inverted V-shaped structures

that are symmetric about the roughness elements' centerlines. These structures could be interpreted as elongated hairpin vortices such as those visualized by Acarlar and Smith (1987), tethered to the roughness elements on their spanwise edges. At $x = 400$ mm the fluctuation intensity decreases as the structures split into as many as four lobes and cover an even larger spanwise region. It is possible that the structures all split into four lobes but that two or three lobes are sometimes observed because of the measurements' limited spanwise resolution. A critical point is well illustrated at in the wake of the second roughness element at $x = 500$ mm. Here the $u'_{\rm rms}$ distribution is split into four nearly identical lobes and these are centered exactly in the regions where the spanwise gradient of the steady streamwise velocity ($\partial U/\partial z$) is a maximum. This indicates that the fluctuations are not unsteady transient disturbances but are likely to be a Kelvin-Helmholz instability that arises at the spanwise inflection points of the streamwise velocity. The behavior for the $Re_k = 264$ is very similar and is therefore omitted from this text for brevity. A second important point is indicated by Fig. 4. Although great attention is given to produce identical roughness elements, there is great deal of variations among roughness elements' fluctuation intensities, as much as an order of magnitude in $u'_{\rm rms}$. Therefore, spanwise phase-locked averaging technique is not used for unsteady fluctuation intensities.

Figure 5 shows the distribution and evolution of $u'_{\rm rms}$ for the transitional configuration, $Re_k = 334$, with the same contour levels used in Fig. 4. It is immediately apparent that both the unsteady fluctuation intensity and the steady disturbance levels are higher than that for the baseline configuration. Immediately downstream of the roughness array, the unsteady velocity fluctuations are concentrated in three regions, one directly above the roughness centerline and two on both sides of the roughness element. These regions are most distinct and symmetric for third and fourth elements from the left. The two lobes located downstream of either side of the roughness element can again be interpreted as the two legs of the horseshoe vortex. At $x = 350$ mm, the unsteady fluctuations are greatly intensified compared to the same streamwise location for the baseline configuration. Additionally, the spanwise region covered by the fluctuations is increased such that the second and third roughness elements' unsteady wakes are joined. At this location, the second roughness element's fluctuations are the most extensive in the wall-normal direction, as they reach the edge of the boundary layer. A stronger inverted V-shaped structure is observed downstream of the rightmost roughness element. At $x = 400$ mm, abrupt changes occur in both the steady and unsteady disturbances. The unsteady wakes of all roughness elements shown in this figure are joined and most of the boundary layer is contaminated by turbulent fluctuations. The mixing downstream of the middle two roughness elements is most severe and the steady velocity contours to from their usual laminar appearance. Further downstream, at $x = 475$ mm, the flow is completely contaminated by unsteady fluctuations with high turbulence levels. The steady velocity contours are strongly affected by turbulent mixing and are well on their way toward a fully developed turbulent boundary layer profile. The maximum $u'_{\rm rms}$ in this figure is 14% of U_∞.

A quantitative assessment of the unsteady disturbances' evolution can be made by defining the total unsteady disturbance energy contained in a single roughness-array wavelength, λ_k. This is computed by integrating the unsteady disturbance energy across one wavelength of the disturbance array and from the wall to the freestream:

$$e_{\rm rms} = \int_0^{\lambda_k} \int_0^{\infty} \left(u'_{\rm rms}\right)^2 d\eta\, dz.$$

It is obvious from Fig. 5 that the middle two roughness elements generate the strongest disturbances and trigger turbulent flow. The second roughness element's wake is selected for data analysis for each of the three roughness array amplitudes. The downstream evolution of $e_{\rm rms}$ generated by this element is shown in Fig. 6. With increasing downstream distance, the unsteady disturbance energy slightly increases and remains constants for $Re_k = 202$ and 264. For the transitional $Re_k = 334$ configuration it experiences exponential growth prior to transition.

The important frequencies associated with the transitional disturbance input can be revealed from the frequency spectrum of the unsteady fluctuations. Figure 7 shows the downstream evolution of the temporal power spectrum along the centerline of the second roughness element's wake for $Re_k = 334$. Each plot represents a particular streamwise location and each curve within a plot represents a particular height in the boundary layer. In the near wake, at $x =$ 310 mm, peaks are observed at 360 and a 720 Hz with the latter surrounded by a band of frequencies from 600 to 800 Hz. This band will be referred to as the 700 Hz band. It is unfortunate that these values are harmonics of 60 Hz but contour plots of the bands' integrated intensities are similar to those in Figs. 4 and 5 and it is concluded that these frequencies are associated with the disturbance input and not electronic noise.

Between $x = 330$ and 360 mm, harmonics of the 700 Hz frequency band start to form as ripples in the high-frequency region of the spectra at different heights. These harmonics increase with increasing downstream distance and gradually give the power spectrum a turbulent appearance. At $x = 350$ mm, the power spectrum at $\eta = 1$ appears almost turbulent whereas the spectrum at $\eta = 2$ still has rippled structure. The spectra at $\eta = 3$ and 4 follow the same trend, lagging the others in x-direction. This suggests that the turbulent fluctuations of roughness induced disturbances propagate from the lower parts of the boundary layer to the upper parts with increasing downstream distance. By $x = 400$ mm, power spectra at all heights indicate a turbulent flow.

Similar to the rms disturbance disturbance energy, e_{rms}, a quantitative assessment of the unsteady disturbance growth can be given for the 700 Hz frequency band using

$$e_{700} = \int_{600\text{ Hz}}^{800\text{ Hz}} \int_0^{\lambda_k} \int_0^{\infty} \text{PSD}(f)\, d\eta\, dz\, df.$$

The downstream evolution of e_{700} for the second roughness element's wake is shown in Fig. 8. First, e_{700} increases with increasing Re_k. Next, the $Re_k = 202$ and 264 configurations' e_{700} grows until $x = 330$ mm then decay somewhat and remain constant for the rest of the streamwise domain. On the other hand, the transitional disturbance input experiences a exponential growth until about $x = 400$ mm and remains fairly constant for the next 75 mm. A plausible interpretation of this behavior is that the near wakes of all three roughness arrays are initially unstable to the 700-Hz disturbance. However, the stationary disturbance decreases rapidly (see Fig. 3) and, at some point, the flow becomes stable to these disturbances and their energy decreases. The exception is the transitional case where $Re_k = 334$. Here, the steady disturbance is sufficiently large that the unsteady disturbances are able to bring about transition before they enter a stable region.

Klebanoff et al. (1992) performed similar experiments using isolated 3.2-mm-high hemispherical and cylindrical roughness elements with diameters of 6.3 mm and 3.2 mm, respectively. Those authors report that bypass transition is observed at $Re_k = 325$ for hemispherical roughness elements and at $Re_k = 450$ for cylindrical roughness elements. In that study, the transition is defined as the first occurrence of turbulent bursts in the oscilloscope with a hotwire positioned on the roughness centerline close to the surface. Klebanoff et al. suggest that the Strouhal number, St, is not a strong function of Re_k, when calculated as $St = f_s \delta^*/U_k$, where f_s is the shedding frequency, δ^* is the displacement thickness and U_k is the flow velocity at roughness height. For hemispherical and cylindrical roughness elements, Klebanoff et al. report Strouhal numbers of 0.3 and 0.25, respectively. However, Klebanoff et al.'s Fig. 23 indicates that for cylindrical roughness elements, St does decrease somewhat with decreasing Re_k as Re_k approaches values used in the current work. The shedding frequency of $f_s = 720$ Hz obtained here corresponds to $St = 0.17$ for Rek=202 which is consistent with a reasonable extrapolation of Klebanoff et al.'s data. Moreover, the height-to-diameter aspect ratio of the cylindrical roughness elements is quite a bit lower in the current work than those used by Klebanoff et al. and this could be another reason for the somewhat lower Strouhal number.

B. Multicomponent Velocities

Multicomponent velocity measurements were performed for the baseline roughness configuration at $x = 310$, 320 and 330 mm. The phase-lock averaged spanwise velocity profiles obtained at these locations are presented in Fig. 9. In each plot, the solid curves represent the spanwise velocity at the location where the curve intersects the plots' abscissa. Positive W velocities are to the right, negative values are to the left and 5% of the freestream speed is indicated by the heavy horizontal line in the upper right corner of each plot. Also included in these plots is the approximate location of roughness element generating the disturbances. Immediately downstream of the roughness at $x = 310$ mm, the spanwise velocity field is non-zero around the downstream of the edges of the roughness. Moving downstream to $x = 320$ mm, the spanwise velocities in these regions increase.

Further downstream at $x = 330$ mm, the spanwise velocity profiles reveal several important features about the origin of roughness-induced transient disturbances. First, it is important to note that the spanwise velocity is zero at the roughness centerline and between the roughness elements which confirms the expected symmertries. W is also zero along both sides of the roughness element. There are two regions on both sides of the roughness centerline that show significant spanwise velocities. These regions are almost perfectly symmetric and terminate exactly at the edge of roughness. On the left-hand-side of the roughness wake, the spanwise velocity value is negative close to the surface, below the roughness height, and positive away from the surface, above the roughness height. On the right-hand-side the behavior is the opposite. This is the signature of a counter rotating vortex system with the vortex on the left

hand side rotating clockwise and the vortex on the right hand side rotating counter clockwise. The rotation directions suggest that these vortices are the legs of a horseshoe vortex system such as those visualized by Acarlar and Smith (1987) and sketched in Fig. 1. Outside of each leg of the primary horseshoe a second weaker pair of vortices can be observed that rotate in the opposite direction of the primary pair.

It is important to note that at $x = 330$ mm the sense of the primary vortex system's rotation is not consistent with what one might expect from the contour plot of the streamwise U velocities given in Fig. 10. This figure shows that the centerline velocity is decelerated relative to the flow between the roughness elements. However, the rotation of the horseshoe vortex would tend to bring high-momentum fluid toward the wall directly behind the roughness element and produce the opposite effect. In fact, this is exactly what is observed in the far wake both in the current work (not shown) and in previous investigations by Kendall (1981) for an isolated element and by White and Ergin (2003) and White et al. (2005) for roughness arrays. In the near wake, the deceleration is the result of a small separated region on the roughness elements' downstream side and it takes a considerable streamwise distance for the action of the horseshoe vortex to overcome this and produce accelerated flow along the centerline. This transition from deceleration to acceleration along the centerline has been identified by Tumin and Reshotko (2004) as one cause for the discrepancy between optimal and realizable transient growth. Transient growth of the stationary disturbance can only begin after the primary vortex overcomes the effect of the decellerated flow just downstream of the roughness element.

IV. Summary and Conclusions

Previous transient growth experiments have concentrated mainly on the steady disturbance field and have resolved some important characteristics such as the effects of roughness height and roughness diameter. The present study is intended to extend these efforts by measuring the unsteady and multicomponent flow fields for moderate- and high-amplitude roughness conditions. Unlike the steady disturbance field, the unsteady disturbance field is observed to be extremely sensitive to variations in roughness amplitudes and the variation of the power spectra amplitudes between different roughness elements are large despite all the efforts to manufacture identical shapes. For this reason, phase-locked averaging technique is not used during unsteady data analysis. Instead, the roughness element with the strongest wake is selected. The unsteady fluctuation intensity and the steady velocity contours are plotted together, revealing signs of hairpin and horseshoe vortices and a Kelvin–Helmholz-type instability mechanism. Bypass transition occurs because of this mechanism at $Re_k = 334$ when the steady disturbance is sufficiently large that the unsteady disturbances grow to transitional amplitudes before they enter as stable region as the stationary disturbance decays. The Strouhal number calculated for the present roughness configurations are consistent with the previous studies.

Although the data for the multicomponent velocity measurements is limited at present, the results are quite interesting. The spanwise velocity measurements clearly show a horseshoe vortex system and this supports the notion that roughness-induced transient growth is consistent with Landahl's (1980) lift-up concept. Multicomponent velocity measurements are critical to an improved understanding of realizable transient growth because it is the streamwise-oriented vortex (i.e., the V' and W' disturbances) that is the initiator of transient growth. Future studies will be concentrated on estimating streamwise and spanwise velocity gradients from experimental data and calculating the wall-normal velocity from the continuity equation. This will provide the necessary initial disturbance conditions for computational works and will form the foundation for meaningful growth predictions for physically realizable disturbances.

Acknowledgments

This work is supported by the Air Force Office of Scientific Research under grant number F49620-02-1-0058 and is managed by Dr. Thomas Beutner. Additionally, the authors wish to thank Sam Cordaro, Wayne Schmidt, John Weber and Ron Hudak of the Case Engineering Services Fabrication Center for their suggestions, cooperation and support. F.G. Ergin acknowledges the Case School of Engineering for its support through a Case Prime Fellowship.

References

Acarlar, M. and C. Smith (1987). A study of hairpin vortices in a laminary boundary layer. Part 1. Hairpin vortices generated by a hemisphere protuberance. *J. Fluid Mech. 175*, 1–41.

Andersson, P., M. Berggren, and D. S. Henningson (1999). Optimal disturbances and bypass transition in boundary layers. *Phys. Fluids 11*(1), 134–150.

Ashpis, D. and E. Reshotko (1990). The vibrating ribbon problem revisited. *J. Fluid Mech. 213*, 531–547.

Ashpis, D. E. and E. Reshotko (1998). Excitation of continuous and discrete modes in incompressible boundary layers. Technical report, NASA TM-1998-208490.

Bruun, H. H. (1995). *Hot-Wire Anemometry Principles and Signal Analysis.* Oxford University Press.

Butler, K. and B. Farrell (1992). Three-dimensional optimal perturbations in viscous shear flow. *Phys. Fluids A 4*(8), 1637–1650.

Ellingsen, T. and E. Palm (1975). Stability of linear flow. *Phys. Fluids 18*, 487.

Farrell, B. F. (1988). Optimal excitation of perturbations in viscous shear flow. *Phys. Fluids 31*, 2093.

Fischer, P. and M. Choudhari (2004). Numerical simulation of roughness-induced transient growth in a laminar boundary layer. AIAA Paper 2004-2539.

Fransson, J. H. M., L. Brandt, A. Talamelli, and C. Cossu (2004). Experimental and theoretical investigation of the non-modal growth of steady streaks in a flat plate boundary layer. *Phys. Fluids 16*(10), 3627–3638.

Grosch, C. E. and H. Salwen (1978). The continuous spectrum of the orr–sommerfeld equation. Part 1. The spectrum and the eigenfunctions. *J. Fluid Mech. 87*, 33–54.

Hinze, J. O. (1959). *Turbulence. An introduction to its mechanism and theory.* New York: McGraw-Hill.

Jørgensen, F. E. (1971). Directional sensitivity of wire and fibre-film probes. *DISA Info. 11*, 31–37.

Kendall, J. (1981). Laminar boundary layer velocity distortion by surface roughness: Effect upon stability. AIAA Paper 81-0195.

Klebanoff, P., W. Cleveland, and K. Tidstrom (1992). On the evolution of a turbulent boundary layer induced by a three-dimensional roughness element. *J. Fluid Mech. 237*, 101–187.

Landahl, M. T. (1980). A note on an algebraic instability of inviscid parallel shear flows. *J. Fluid Mech. 98*, 243–251.

Luchini, P. (2000). Reynolds-number-independent instability of the boundary layer over a flat surface: Optimal perturbations. *J. Fluid Mech. 404*, 289–309.

Press, W. H., S. A. Teukolsky, W. T. Vetterling, and B. P. Flannery (1992). *Numerical Recipes in C* (2 ed.). Cambridge: Cambridge University Press.

Reshotko, E. (2001). Transient growth—A factor in bypass transition. *Phys. Fluids 13*(5), 1067–1075.

Rice, J. M. (2004). Roughness receptivity and scaling of non-optimal transient disturbances. Master's thesis, Case Western Reserve University.

Schmid, P. J. and D. S. Henningson (2001). *Stability and transition in shear flows*. New York: Springer.

Sedney, R. (1973). A survey of the effect of small protuberances on boundary-layer flows. *AIAA J. 11*, 782–92.

Tumin, A. (2003). Multimode decomposition of spatially growing perturbations in a two-dimensional boundary layer. *Phys. Fluids 15*(9), 2525–2540.

Tumin, A. and E. Reshotko (2001). Spatial theory of optimal disturbances in boundary layers. *Phys. Fluids 13*(7), 2097–2104.

Tumin, A. and E. Reshotko (2004). The problem of boundary-layer flow encountering a three-dimensional hump revisited. AIAA Paper 2004-0101.

White, E. B. (2002). Transient growth of stationary disturbances in a flat plate boundary layer. *Phys. Fluids 14*(12), 4429–4439.

White, E. B. and F. G. Ergin (2003). Receptivity and transient growth of roughness-induced disturbances. AIAA Paper 2003-4243.

White, E. B. and F. G. Ergin (2004). Using laminar-flow velocity profiles to locate the wall behind roughness elements. *Exp. Fluids 36*(2), 805–812.

White, E. B. and E. Reshotko (2002). Roughness-induced transient growth in a flat-plate boundary layer. AIAA Paper 2002-0138.

White, E. B., J. M. Rice, and F. G. Ergin (2005). Receptivity of stationary transient disturbances to surface roughness. *Phys. Fluids*. Submitted.

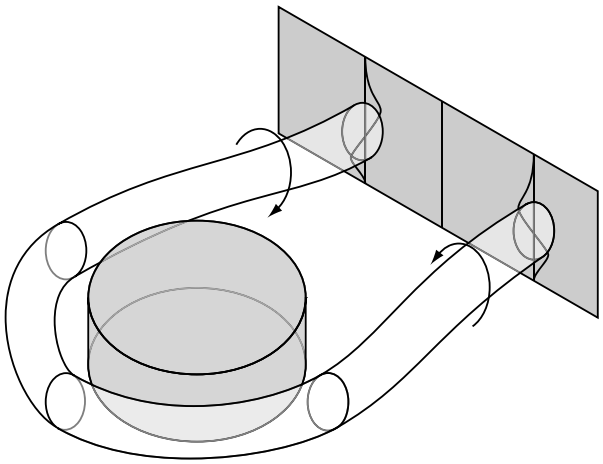

Figure 1: Schematic illustration of the horseshoe vortex about a cylindrical roughness element. The curves on the plane to the right of the figure indicate profiles of the steady spanwise velocity.

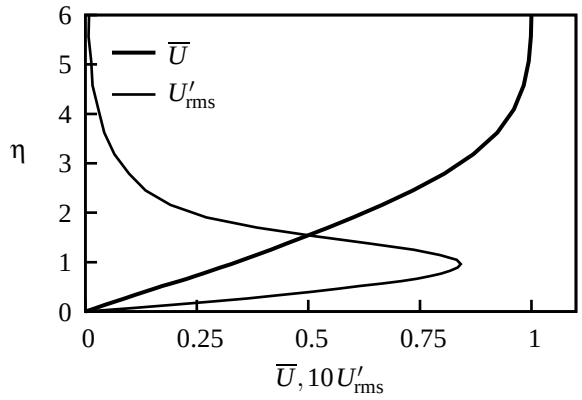

Figure 2: Basic state and steady disturbance profiles for $x = 310$ mm, $Re_k = 202$.

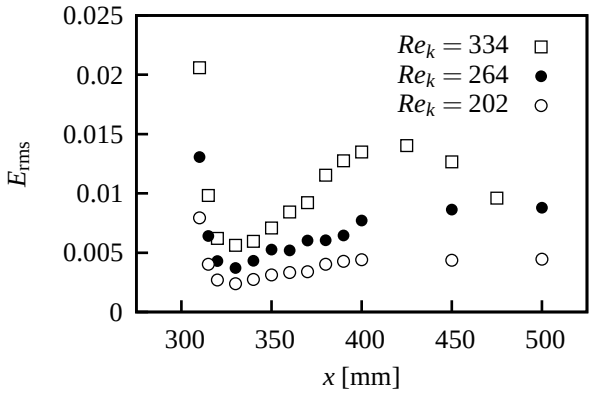

Figure 3: Streamwise evolution of the steady disturbance energy, E_{rms}.

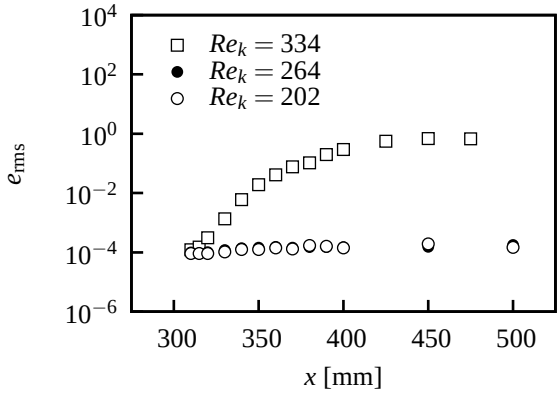

Figure 6: Streamwise evolution of the unsteady disturbance energy, e_{rms}.

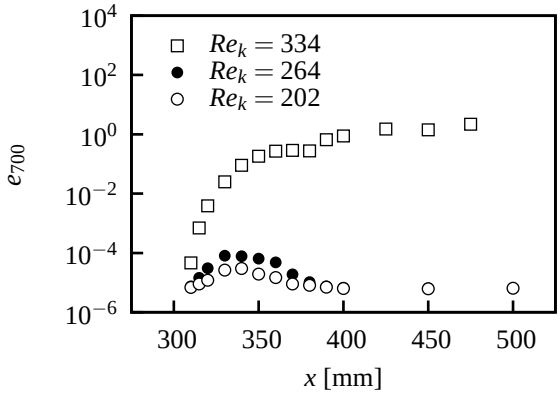

Figure 8: Streamwise evolution of the 700 Hz band's disturbance energy, e_{700}.

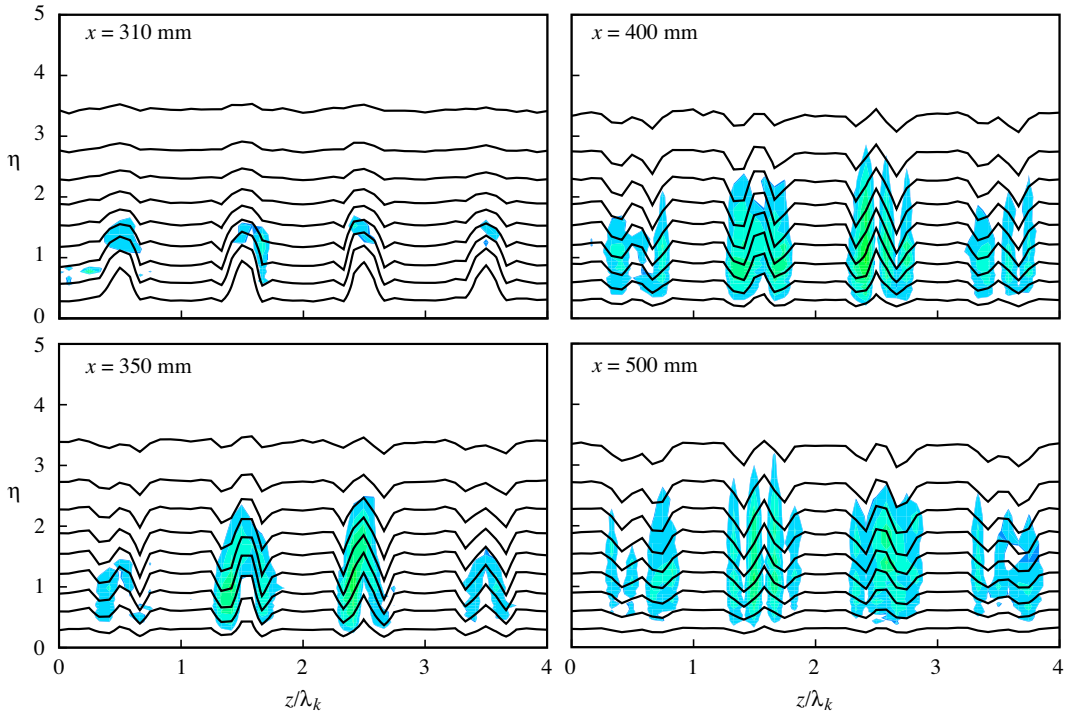

Figure 4: Unsteady velocity fluctuation intensity evolution for $Re_k = 202$.

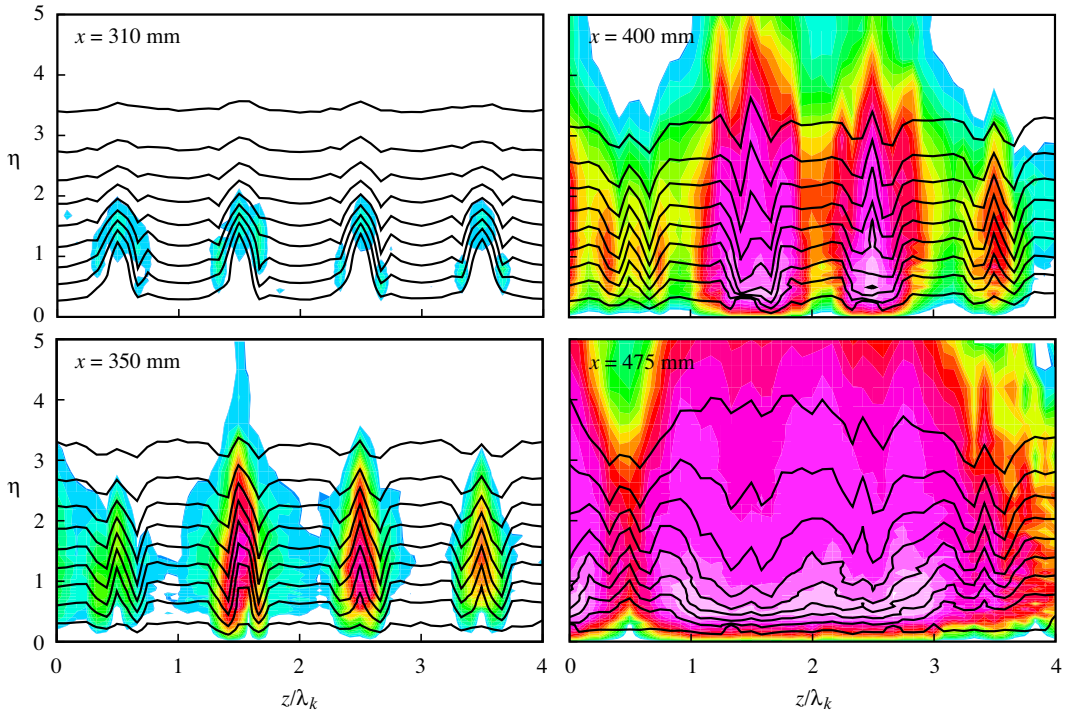

Figure 5: Unsteady velocity fluctuation intensity evolution for $Re_k = 334$.

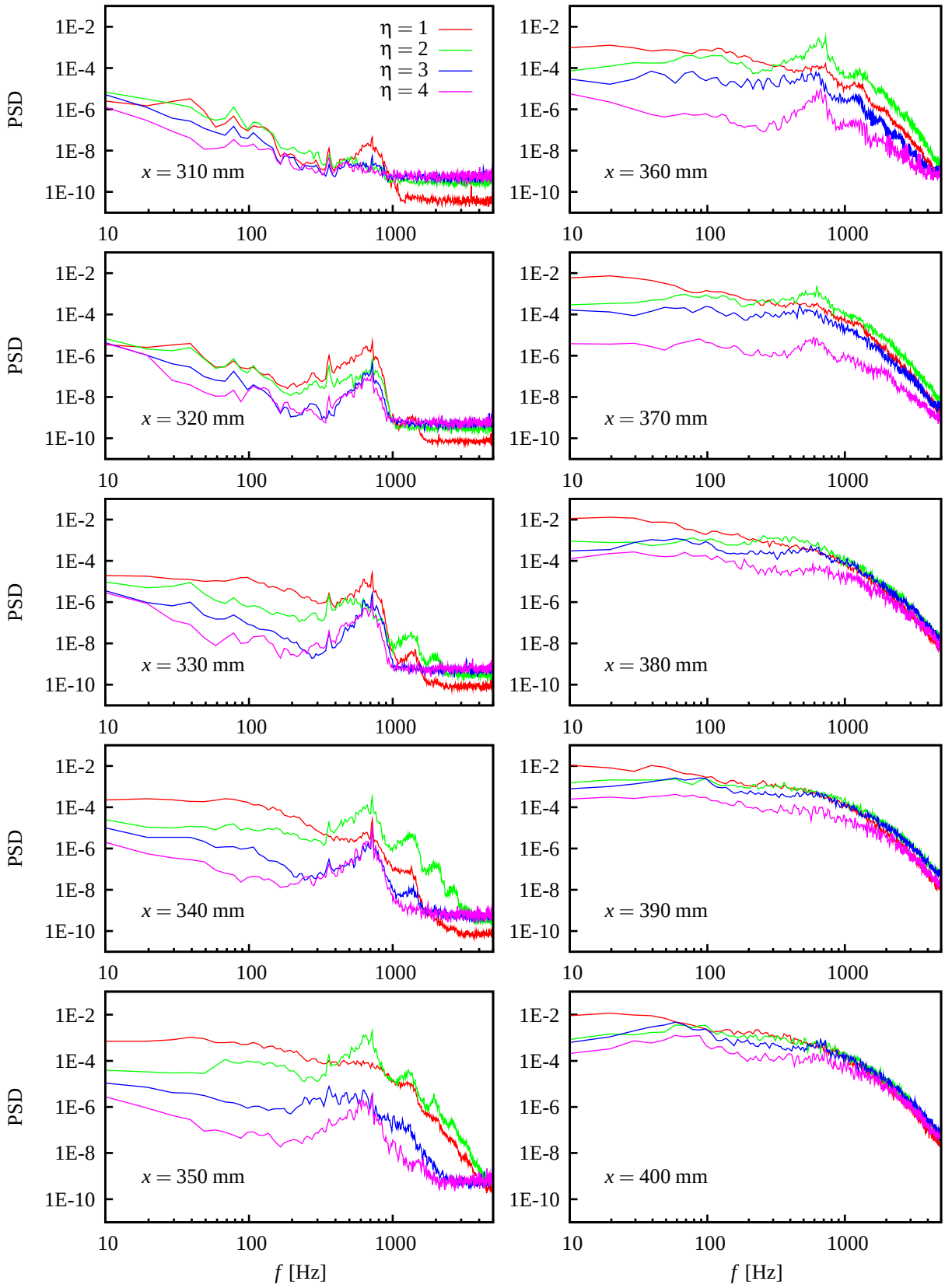

Figure 7: Temporal power spectra of the unsteady disturbances for $Re_k = 334$.

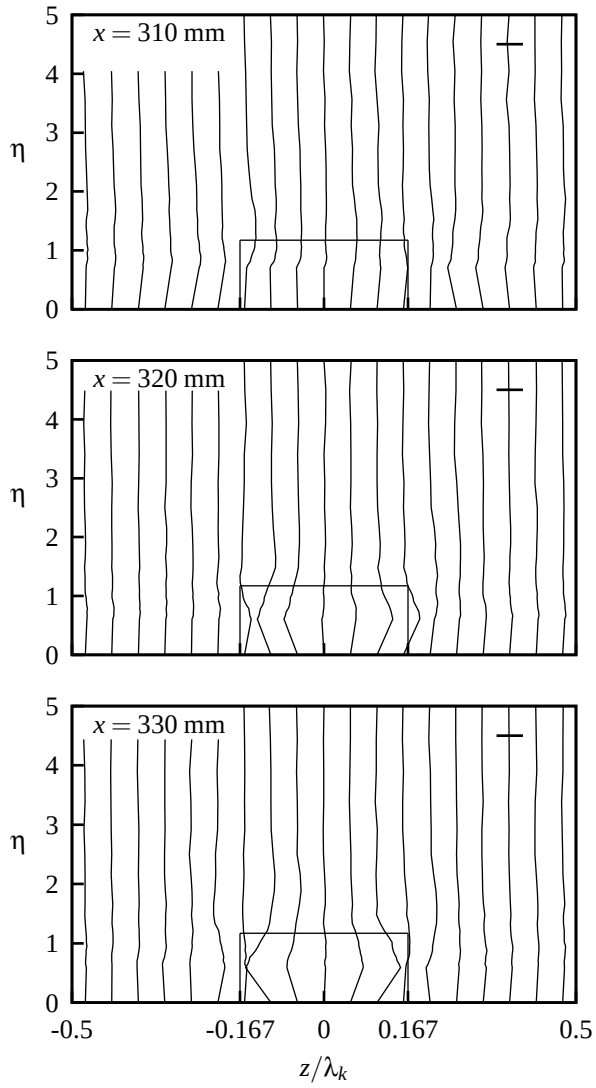

Figure 9: Wall-normal profiles of spanwise velocity for $Re_k = 202$. The rectangular boxes indicate the approximate size and location of the roughness elements and the heavy horizontal line indicates 5% U_∞.

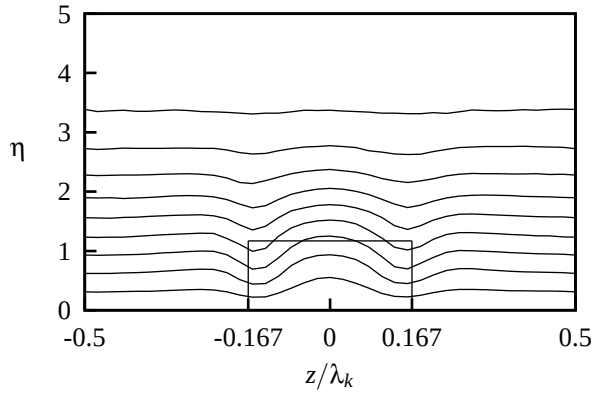

Figure 10: Streamwise velocity contours for $x = 330$ mm, $Re_k = 202$. Contour lines indicate 10% increments of U_∞.